

Continuously trapped matter-wave interferometry in magic Floquet-Bloch band structures

Xiao Chai,¹ Jeremy L. Tanlimco,¹ Eber Nolasco-Martinez,¹ Xuanwei Liang,¹ E. Quinn Simmons,¹ Eric Zhu,¹ Roshan Sajjad,¹ Hector Mas,¹ S. Nicole Halawani,¹ and David M. Weld^{1,*}

¹*Department of Physics, University of California, Santa Barbara, California 93106, USA*

Trapped matter-wave interferometry offers the promise of compact high-precision local force sensing. However, the trap itself can introduce new systematic errors which are absent in traditional free-fall interferometers. We describe and demonstrate a novel Floquet-engineered platform for compact, continuously trapped atom interferometry which is intrinsically robust against trap noise and beamsplitter pulse duration. A non-interacting degenerate quantum gas undergoes position-space Bloch oscillations through an amplitude-modulated optical lattice, whose resulting Floquet-Bloch band structure includes Landau-Zener beamsplitters and Bragg mirrors, forming the components of a Mach-Zehnder interferometric force sensor. We identify, realize, and experimentally characterize magic band structures, analogous to the magic wavelengths employed in optical lattice clocks, for which the interferometric phase is insensitive to lattice intensity noise. We leverage the intrinsic programmability of the Floquet synthesis approach to demonstrate a variety of interferometer structures, highlighting the potential of this technique for quantum force sensors which are tunable, compact, simple, and robust.

Interferometry has been a tool of discovery in physics for centuries [1, 2]. While originally demonstrated with photons, the wave-particle duality [3] of matter enables the realization of interferometers in electrons [4], neutrons [5], atoms [6], and molecules [7]. The interferometric sensitivity is set by the spacetime area enclosed by the interferometer loop and thus scales quadratically with freefall time for untrapped particles. This has driven the precision frontier towards large-scale experiments featuring 100-meter-scale drop towers [8] or even low Earth orbit [9]. In contrast, continuously-trapped interferometers can reach very large spacetime areas in the Earth's gravity field without requiring long freefall time, large experimental size, or spaceflight, and offer the practical advantages of compactness and truly local sensing [10–18]. In particular, spatially periodic trapping potentials, such as those produced by optical lattices, support Bloch oscillations [19, 20] that naturally localize atoms for high-precision local measurements. However, instabilities in the trapping potential result in dephasing; this primary limitation of trapped matter-wave interferometers can be partly mitigated by resonant optical mode filtering [21] or differential measurement schemes [17].

In this work we describe and experimentally characterize a new and highly flexible class of atom interferometer based on position-space Bloch oscillations of trapped non-interacting Bose-condensed lithium through loops in a Floquet-engineered optical lattice band structure [22–25]. The sensitivity of this interferometer scales inversely with the applied force, making it especially suitable for detection of weak forces. Instead of using traditional Raman or Bragg pulses, matter-wave splitting and recombination is realized via tunable Landau-Zener transitions at quasimomentum-selective Floquet-Bloch band cross-

ings. This makes the interferometer intrinsically insensitive to fluctuations in initial momentum, pulse duration, and laser phase. Immunity against trap intensity fluctuations is achieved by the use of an infinite family of magic Floquet-Bloch band structures, which generalize the concepts of magic wavelengths and magic lattice depths [26] and which we experimentally verify offer first-order insensitivity to lattice amplitude noise. These advantages are a consequence of the remarkable degree of design flexibility offered by Floquet band engineering, which takes inspiration from related concepts in condensed matter physics [27, 28] and photonics [29, 30] and enables the synthesis of a wide variety of interferometer loops with different characteristics and tunable force response. A key virtue of this interferometer class is its simplicity and programmability: it requires only a single optical lattice without cavity mode filtering, and can be widely and instantly reconfigured by changing only a radiofrequency (RF) modulation waveform.

The central component of our interferometer is a horizontal one-dimensional optical lattice amplitude-modulated to hybridize the Bloch bands (Fig. 1). The lattice potential takes the form $V(x, t) = -(V_0 + \delta V \sin \omega t) \cos^2(k_L x)$, where V_0 is the static lattice depth, δV and ω are the modulation depth and frequency respectively, $k_L = 2\pi/\lambda$ is the lattice laser wavenumber, and $\lambda = 1064\text{ nm}$ is the lattice laser wavelength. This yields a spatially and temporally periodic single-particle Hamiltonian to which Floquet-Bloch theory can be readily applied [22]. As shown in Fig. 1c, the modulation opens up gaps between Floquet-Bloch quasienergy bands when the resonance condition $E_{n,q_r} - E_{n',q_r} = \hbar\omega$ is satisfied, where $E_{n,q}$, $E_{n',q}$ are the bare Bloch band energies for bands labeled n and n' (henceforth S, P, D , etc., following orbital notation), q is the quasimomentum, q_r is the resonant quasimomentum, and \hbar is the reduced Planck constant. When a matter wave in

* weld@physics.ucsb.edu

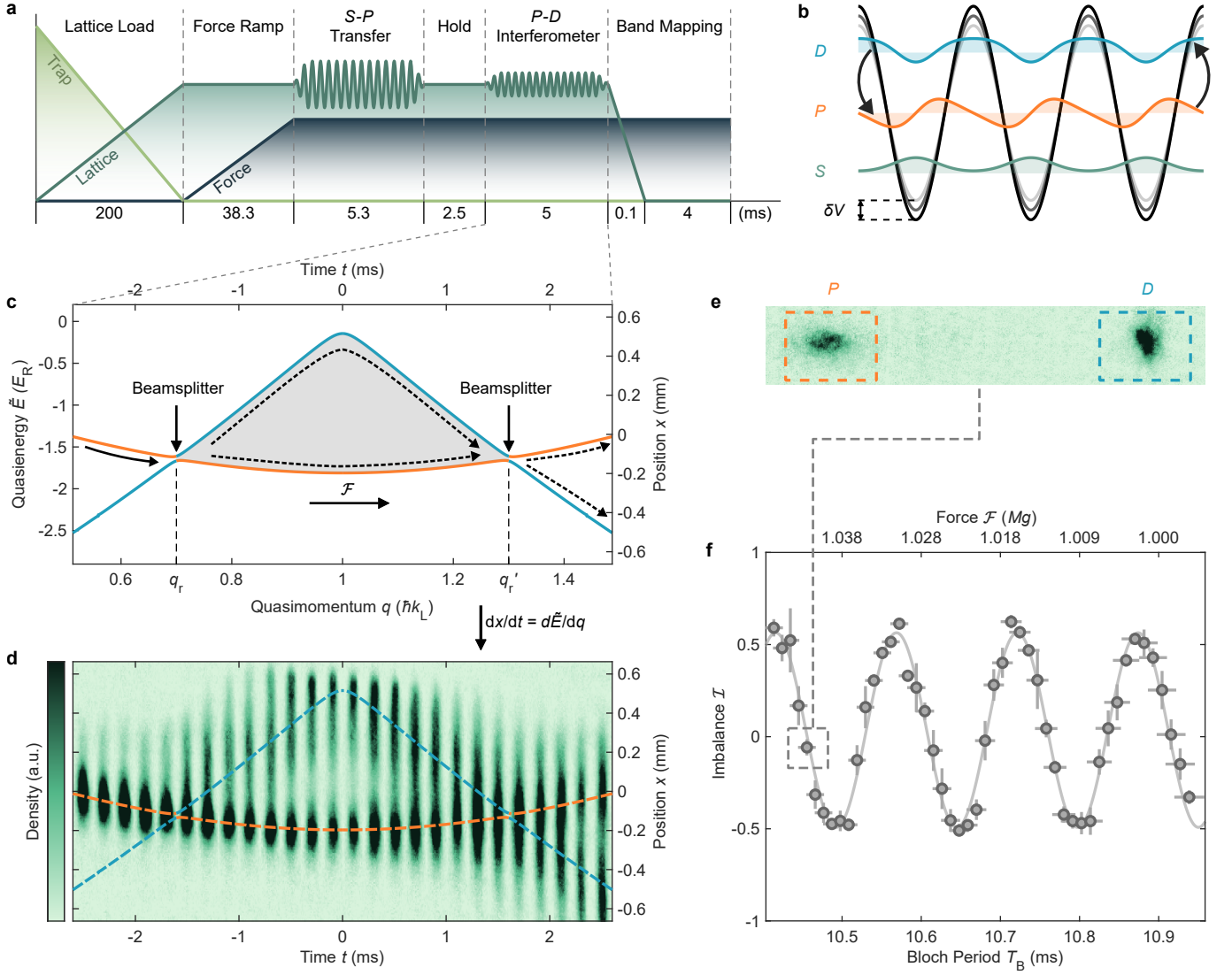


FIG. 1. **Floquet-Bloch matter-wave interferometry.** (a) Experimental sequence. (b) Resonant amplitude modulation of the optical lattice hybridizes the P and D (second and third) Bloch bands. (c) Interferometric loop formed by the Floquet-Bloch band structure and Landau-Zener beamsplitters. A matter wave Bloch oscillates through the paths indicated by the arrows in response to a force \mathcal{F} . The color of the Floquet-Bloch bands corresponds to the Bloch states in (b) with maximal wavefunction overlap. (d) Time sequence of *in situ* images of a condensate traversing the interferometric loop. The space-time trajectories map out the Floquet-Bloch band structure. (e) Band-mapping clearly separates the two output port populations. (f) Output population imbalance \mathcal{I} versus applied force. Mg is the mass times the local gravitational acceleration, used here only as a force scale; the lattice is horizontal. In all figures, vertical error bars are the standard error of 3 repeated measurements and horizontal error bars are the estimated uncertainties from calibration fits (Supplementary Information).

one band traverses the avoided crossing at $q = q_r$, it coherently splits into a superposition state between the two output bands [31–33]. By tuning the modulation depth δV , the Landau-Zener transition probability p can be adjusted to 50% [34]. Arbitrary synthesis of the RF modulation waveform allows fully programmable manipulation of both the location and strength [34] of all such avoided crossings between quasienergy bands: these will become the beamsplitters and other control elements comprising the interferometer.

In the presence of a force \mathcal{F} along the lattice direction,

the acceleration theorem [35] guarantees that the quasi-momentum q of a matter wave evolves as $q(t) = q(0) + \mathcal{F}t$, with the Bloch period defined by traversal of the entire Brillouin zone:

$$T_B = \frac{2\hbar k_L}{\mathcal{F}}. \quad (1)$$

Crucially, this Stückelberg-type evolution in quasienergy and quasimomentum [36, 37] also results in motion in real space: the mean position $x(t)$ of a wavepacket in a Floquet-Bloch band with quasienergy dispersion relation $\tilde{E}(q)$ evolves according to the group velocity as

$dx/dt = d\tilde{E}/dq$ [20]. The displacement associated with such position-space Bloch trajectories can be especially large for light atoms like lithium; separations on the millimeter scale are straightforwardly attained. This means that by adjusting the modulation waveform to synthesize a particular Floquet-Bloch band structure between two Landau-Zener avoided crossings, we are synthesizing a particular spacetime trajectory for the atoms in the interferometer loop: the quasienergy band dispersion is simply a scaled image of the center of mass time evolution [23], as shown in Fig. 1c-d. Components of the atomic wavefunction which are separated at an initial Landau-Zener beamsplitter and traverse the two arms of such a loop accumulate a relative dynamical phase which depends on the applied force. This phase is measured by interfering the two pathways at the second beamsplitter, forming a Landau-Zener-Stückelberg-Majorana interferometer [38, 39] and resulting in a final population imbalance between the two output bands (Supplementary Information) $\mathcal{I} = p_L - p_U \approx C \cos \phi_{\text{Int}}$, where $L(U)$ denotes the lower (upper) Floquet-Bloch band, $p_{L(U)}$ the corresponding population fractions, and the ideal contrast $C = 4p(1-p)$. The interferometer phase is $\phi_{\text{Int}} = \phi_{\text{Dyn}} + 2\phi_{\text{Sto}}$, where $\phi_{\text{Sto}} \in [-\pi/2, -\pi/4]$ is the Stokes phase imparted by one of the Landau-Zener transitions, which depends only weakly on the applied force (Supplementary Information). ϕ_{Dyn} is the differential dynamical phase

$$\phi_{\text{Dyn}} = \frac{T_B}{2\hbar^2 k_L} \int_{q_r}^{q_r' = q_r + \Delta q} dq \left(\tilde{E}_{U,q} - \tilde{E}_{L,q} \right), \quad (2)$$

where $\tilde{E}_{L(U),q}$ denotes the quasienergy. The dynamical phase is proportional to T_B and thus $1/\mathcal{F}$; the force sensitivity scales linearly with the energy-momentum area enclosed by the interferometer loop.

The experimental apparatus with which we realize this interferometer builds upon previous work (see [23] and Methods). A ^7Li Bose-Einstein condensate (BEC) is prepared in the $|f, m_f\rangle = |1, 1\rangle$ magnetically sensitive state within a crossed dipole trap. To eliminate interaction-induced dephasing [17], we apply a magnetic field of 543.6 G to tune the s -wave scattering length to zero [40] using lithium's shallow Feshbach zero-crossing. The atoms are then adiabatically loaded into the ground band of a horizontal one-dimensional optical lattice (Fig. 1a) with a lattice depth $V_0 = 8.45 E_R$, where $E_R = \hbar^2 k_L^2 / 2M$ is the recoil energy, and M is the atomic mass. Subsequently, we ramp up a magnetic field gradient effecting a nearly uniform force \mathcal{F} along the lattice direction to initiate Bloch oscillations. A strong 120 kHz lattice amplitude modulation pulse is then applied to transfer the atoms from the S to P band with 100% Landau-Zener probability (Methods). This initial transfer allows us to implement the interferometer using P - D hybridized Floquet-Bloch bands, the lowest combination which supports magic band structures. After a 2.5 ms hold time, a 127.438 kHz modulation is ramped up within 100 μs

to load the atoms adiabatically into the upper P - D hybridized Floquet-Bloch band. The modulation depth is calibrated to be $\delta V = 0.35 E_R$ for 50-50 beam splitting (Supplementary Information). The modulation is sustained for 4.8 ms, during which time the atoms traverse the Brillouin zone edge and complete the interferometer loop at the second crossing. The second crossing is created by the same modulation and therefore is mirrored around the zone edge from the first crossing; this allows the interferometer loop to close. Figure 1d shows a series of snapshots capturing the atoms traversing the interferometer loop, where the center-of-mass motion clearly maps out the Floquet-Bloch band structure [20, 23]. Finally, the modulation is ramped down in 100 μs to convert atoms in upper (lower) Floquet-Bloch bands back into the static P (D) Bloch bands. We perform band-mapping [41] and absorption imaging to read out the band populations with high fidelity (Fig. 1e). Figure 1f demonstrates a functioning interferometer, displaying a measured interference fringe in which the population imbalance depends sinusoidally on the inverse of the applied force \mathcal{F} .

In addition to force, the differential dynamical phase in general also depends sensitively on lattice depth. If this were always the case it would spoil the performance of force sensors of this type [42]. Fortunately, the flexibility and large available parameter space of multi-frequency Floquet band engineering allows for the design and creation of magic band structures which null out the lattice depth dependence. The condition for magicness of a Floquet-Bloch band loop is $\partial\phi_{\text{Int}}/\partial V_0 = 0$. This condition cannot be realized in any simple loop whose constituent bands include the ground (S) band. The reason for this is that the perturbative effect of nonzero V_0 on the free-particle parabolic dispersion serves to repel the different bands; since the S band uniquely only experiences repulsion from above, its energy monotonically decreases with increasing lattice depth (and more steeply than any other band), precluding the existence of any nonzero V_0 for which the energy difference with another band has zero derivative [26]. Thus, the simplest pair of bands which can realize a “magic-depth” interferometer are the P and D bands. For example, as demonstrated numerically in Fig. 2a, the magic condition is realized for a P - D interferometric loop extending from $q_r = 0.8 \hbar k_L \rightarrow q_r' = 1.2 \hbar k_L$ at lattice depth $V_0^M \approx 8.85 E_R$. This approach can be generalized to different loop areas and interferometer geometries: such magic band structures can be found for essentially any quasimomentum range (Supplementary Information) and any set of constituent excited bands.

To test the predicted magic band structure, we first measure the population imbalance at fixed force and modulation waveform across a range of lattice depths near this value. The results, shown in Fig. 2b, indeed indicate a broad region with $\partial\phi_{\text{Int}}/\partial V_0 \approx 0$ centered on $V_0 = 8.85 E_R$. To probe directly the performance of magic versus non-magic band structures, we measure

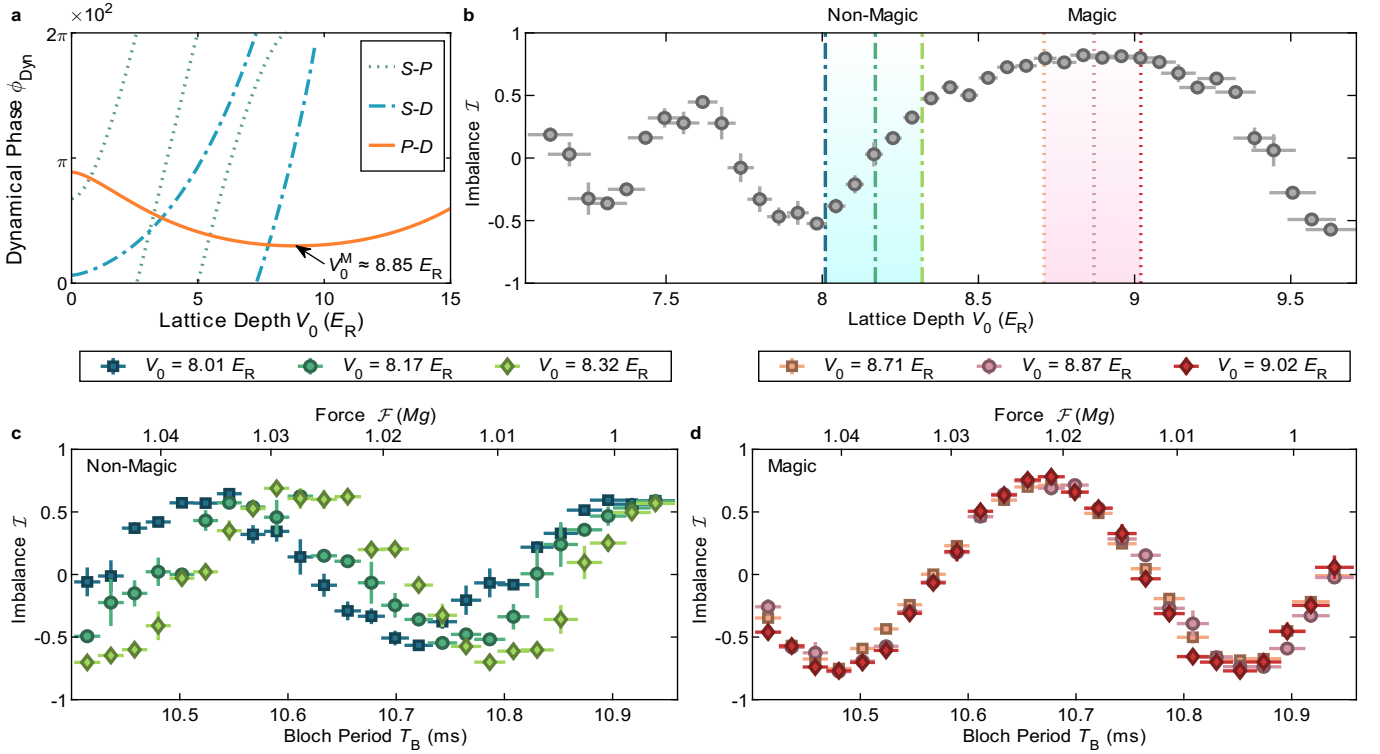


FIG. 2. **Magic band structures.** (a) Numerically calculated dynamical phase (Eq. 2) modulo $2\pi \times 10^2$ for $S-P$, $S-D$, and $P-D$ interferometric loops (with 100 kHz, 190 kHz, and 143 kHz drives, respectively) as a function of lattice depth for $T_B = 10.7$ ms estimated with static band energies; only the $P-D$ loop exhibits a magic condition at nonzero $V_0^M \approx 8.85 E_R$. (b) Output population imbalance at $T_B = 10.70$ ms as a function of lattice depth. Vertical dashed (dotted) lines indicate the lattice depths chosen for force measurements far from (close to) the magic condition. (c-d) Imbalance as a function of applied force away from (c) and close to (d) the magic condition at the aforementioned lattice depths.

force scans for three closely spaced lattice depths away from the magic condition (Fig. 2c) and for three closely spaced lattice depths centered at the magic condition (Fig. 2d). Measurements far from the magic condition exhibit sensitive dependence on lattice depth and greater fluctuations in imbalance for a given lattice depth; in contrast, force measurements at or near the magic condition are quiet and consistent across a range of lattice depths. These results clearly demonstrate both the successful experimental implementation of magic Floquet-Bloch band synthesis and its utility for force sensing.

One key motivation for continuously trapped atom interferometry is the ability, in principle unlimited by geometrical constraints, to scale up the spacetime area of the interferometer loop to increase sensitivity. To probe such scaling, we use the intrinsic flexibility of Floquet-synthesized interferometry to create a sequence of interferometers with increasing spacetime loop area. Specifically, we measure interference fringes produced using loops which subtend spans of quasimomenta $\Delta q = q'_r - q_r$ ranging from $0.2 \hbar k_L$ to $1 \hbar k_L$, keeping the interferometer loop symmetric about the Brillouin zone edge. This probes the performance of interferometers with different momentum-space beamsplitter separations. For each loop size, we recalculate the magic condition and ad-

just the lattice depth accordingly. At the magic condition, the range of acceptable lattice depth fluctuations decreases with increasing loop size (Fig. 3b), but for all measurements remains comfortably above the experimentally achievable lattice depth stability. As shown in Fig. 3a, the measured interference fringes become finer as the loop area increases, indicating an increased force response. We believe the reduction of fringe contrast at higher Δq is induced mainly by technical issues including residual magnetic field curvature and imperfections in the transverse lattice mode; this is a topic of ongoing investigation. Fig. 3c shows the inverse of the measured fringe period, which is proportional to the force sensitivity, as measured by sinusoidal fits for each interferometer loop. The results match the analytical theory without any fitting parameters. These data clearly demonstrate a well-understood path to scaling up the force sensitivity in continuously-trapped interferometers by increasing loop area.

Beyond this straightforward increase in beamsplitter separation, the inherent programmability and power of Floquet band engineering also offer a wide variety of other methods to enhance or tune the performance of trapped matter-wave interferometers. Possibilities include the use of switchable or pulsed beamsplitters, the

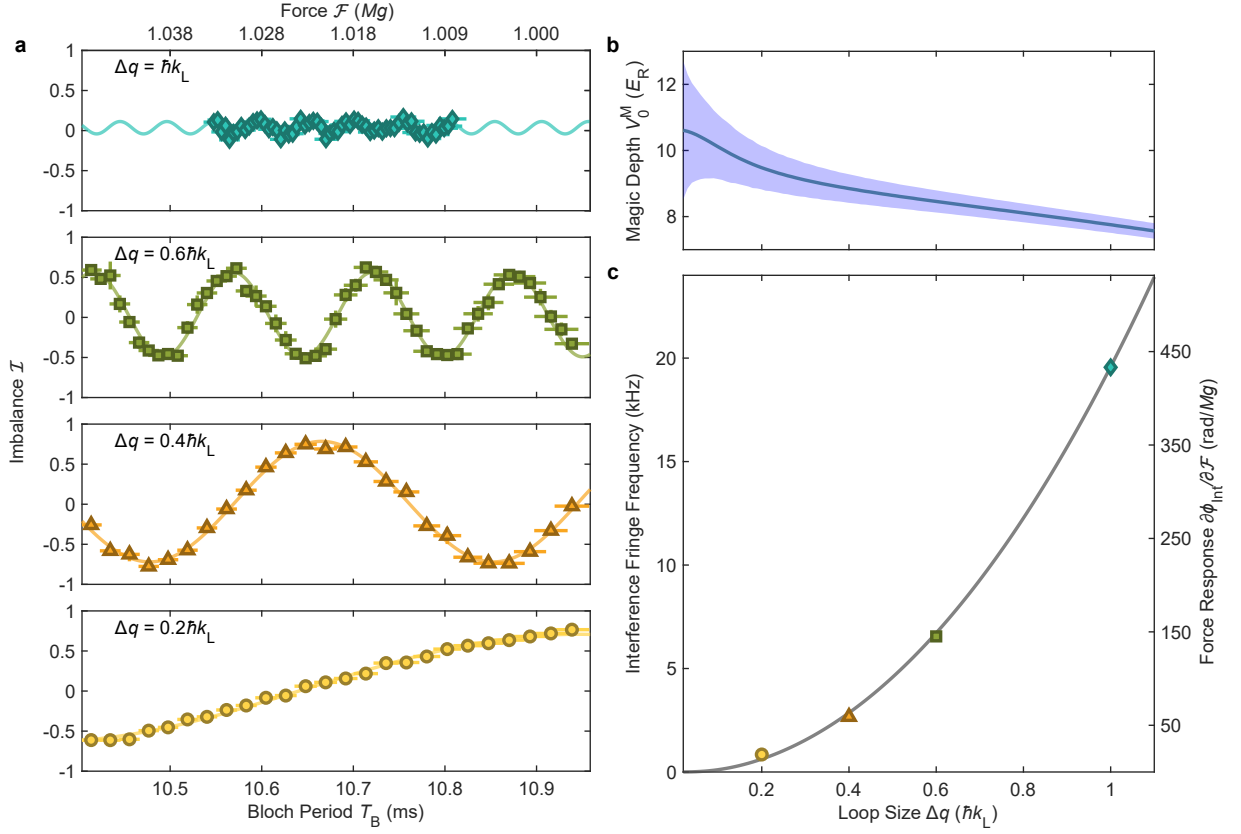


FIG. 3. **Tuning the interferometer response.** (a) Interference fringes for varying loop sizes $\Delta q = q'_r - q_r$, each at the respective magic condition. Solid lines are sinusoidal fits. (b) Theoretically calculated magic depth as a function of loop size. Boundaries of the shaded area mark the lattice depth where the interferometer phase deviates by $\pi/4$. (c) Interferometric response as a function of loop size as defined by the fringe frequency. Data points represent fit results from (a), and the solid line is the theoretical prediction obtained from the fit-parameter-free analytical theory. The corresponding force response is calculated at $\mathcal{F} = Mg$.

inclusion of higher bands beyond D , multifrequency Floquet band engineering, and coherent control of the beam-splitting phase. The final set of experiments we describe explores and demonstrates all these capabilities, stocking a versatile toolbox for programmable trapped matter-wave interferometry.

In the initial such experiment, we address a key limitation of the Floquet band engineering approach to matter-wave interferometry: any modulation frequency which resonantly couples two bands (say, P and D) at a particular quasimomentum will in general also resonantly couple to other bands at different quasimomenta. Such couplings give rise to undesired “leaks” to other states, resulting in parasitic interferometers and reduced contrast. Undesired couplings thus can severely limit the design space for Floquet band interferometers, and become unavoidable for larger-area loops. The problem is illustrated in Fig. 4a, which shows the dressed energy band structure of an interferometer subtending about half a Brillouin zone in quasimomentum [43]. The modulation frequency used to create the beamsplitters by coupling the P and D bands at about 0.5 and $1.5\hbar k_L$ also resonantly couples both the D and F bands and the P and

F bands, at different values of quasimomenta within the interferometer loop. While not shown, higher bands beyond F are also coupled in this range via multiphoton transitions. The modulation scheme in Fig. 4a shows the simplest way around this problem: smoothly turn on and off the modulation so that the bands are only coupled during the beamsplitting operation. Fig. 4b shows a fringe measured in this rather large-area interferometer using pulsed beamsplitters, demonstrating that switchable couplings can be implemented without compromising interferometer performance. This greatly opens up the possible design space for dressed-band interferometry, for instance by allowing loops to extend over multiple Brillouin zones.

Of course, coupling to additional higher bands is not always undesirable; in fact it can be used to design interferometers with enhanced loop area and force sensitivity. Fully flexible use of this capability requires the ability to program arbitrary interband coupling strengths and quasimomenta, which in turn requires the simultaneous use of multiple modulation frequencies. Fig. 4c shows the quasienergy band structure (calculated using many-mode Floquet theory [44]) of an experiment demonstrating this

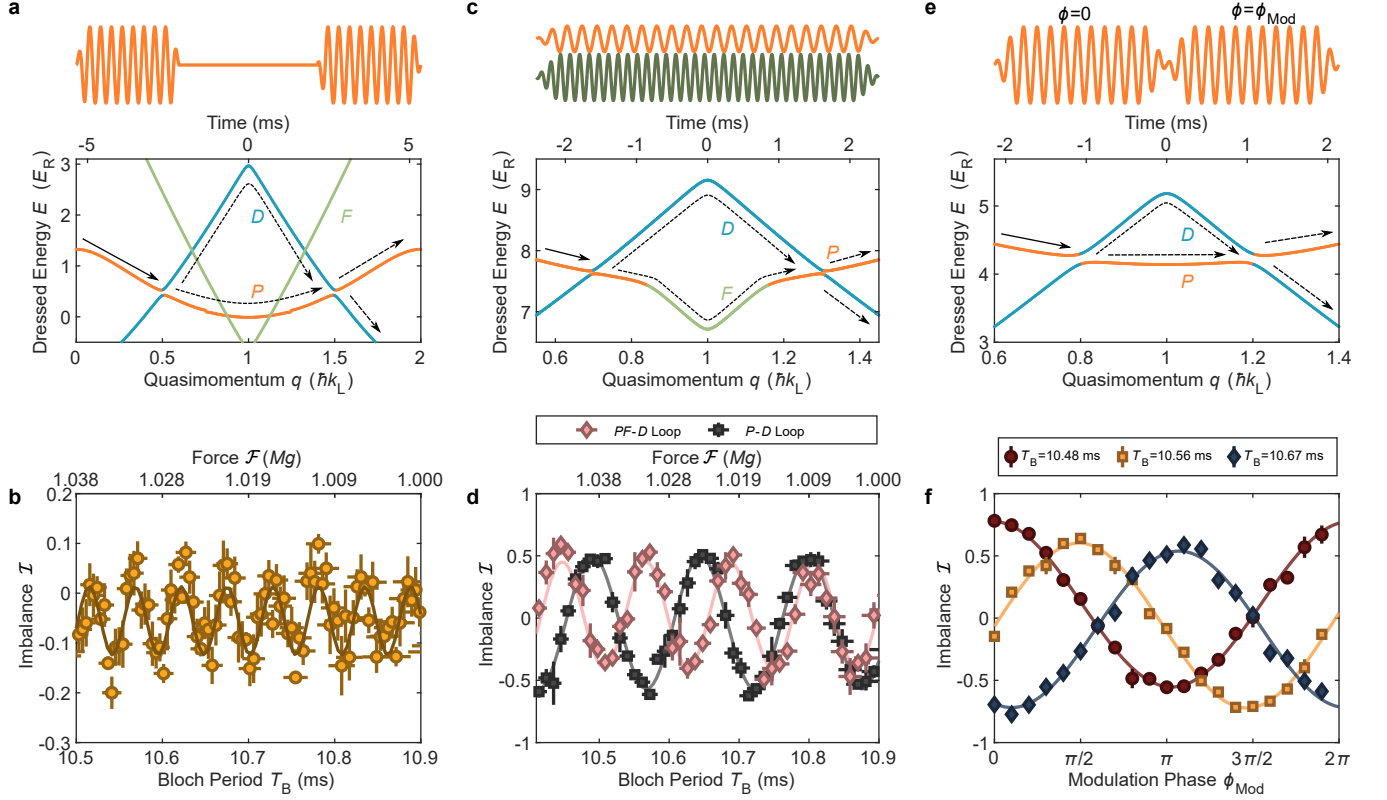


FIG. 4. **Programmable Floquet synthesis of various interferometer structures.** (a) Dressed energies of the $\Delta q = \hbar k_L$ loop and the corresponding modulation waveform. The modulation is pulsed to avoid coupling with the F band. (b) Interferometric fringe generated by the temporally separated pulses. (c) Dressed energies and modulation waveform of the $\Delta q = 0.6 \hbar k_L$ loop in the presence of a second 196 kHz drive (dark green), which hybridizes the P and F bands. (d) Interferometric fringes with and without the second drive. (e) Dressed energies and modulation waveform of the $\Delta q = 0.4 \hbar k_L$ interferometer loop. The phase of the second pulse is shifted by ϕ_{Mod} relative to the first. (f) Output population imbalance as a function of ϕ_{Mod} for three different forces.

capability. We modify a loop with $\Delta q = 0.6 \hbar k_L$ by applying an additional strong modulation at 196 kHz to hybridize the P and F bands at quasimomenta $0.85 \hbar k_L$ and $1.15 \hbar k_L$, with approximately 100% Landau-Zener transition probability. The loop which includes the F band has a larger area and should be more sensitive to the applied force than the original P - D loop. Measured interference fringes for the two interferometers, shown in Fig. 4d, demonstrate the predicted decrease in fringe period and increase in sensitivity. This result demonstrates that arbitrary multi-frequency modulations can be used to construct tailored band structures to control and optimize loop geometry and response of trapped matter-wave interferometers.

Finally, to optimize the response of an interferometer to arbitrary perturbations it is helpful to be able to tune the overall phase of the interference fringes. This is straightforwardly accomplished for trapped Floquet-band matter-wave interferometers by adjusting the phase of the lattice modulation waveform which creates one of the beamsplitters. Fig. 4e diagrams such an experiment in a P - D interferometer with $\Delta q = 0.4 \hbar k_L$, which builds

on the separated-pulse interferometry demonstrated in Fig. 4a-b with the addition of a phase shift between the two beamsplitter modulation pulses. Fig. 4f shows the results: for three different overall forces, scanning the phase of the second beamsplitter pulse shifts the fringe by up to 2π . This demonstration of coherent control of beamsplitter phase is useful for determining the contrast when the force cannot be easily scanned, and enables straightforward biasing of interferometer response to the point of maximum sensitivity. Moreover, this method serves as a practical tool for characterizing interferometer stability for a fixed set of parameters. Extended Data Fig. 1 shows that the phase-scan fringes are nearly immune to 10% variations in initial quasimomenta and pulse durations, highlighting the intrinsic robustness inherited from utilizing Landau-Zener transitions for beamsplitters, as achieving the desired transition probability (and thus the maximal contrast) only depends on the pulse overlapping the crossing at some point rather than its exact duration.

We have described and experimentally demonstrated a simple, versatile, and extensible class of trapped matter-wave interferometer constructed from magic Floquet-

Bloch band structures in an amplitude-modulated optical lattice. Key virtues of this approach include compactness, flexibility, high ultimate sensitivity unlimited by device size, and intrinsic robustness against trap-induced dephasing and pulse errors. The force sensitivity in the weak-force regime improves as $1/\mathcal{F}$, a feature that could be exploited in more generality by introducing an accelerated lattice to realize a frame transformation and cancel part of the force. Compact trapped interferometers suitable for weak force measurement may find application in fifth force searches or similar probes of physics beyond the standard model [45–48].

The ultimate limits on the sensitivity of this technique remain to be explored. While in the experiments we present the coherence was limited by technical imperfections like residual magnetic field curvature and lattice beam mode quality, this can be straightforwardly improved. Possible avenues for such improvements include using higher-order magic band structures which cancel additional systematics, magnetically insensitive states or isotopes with intrinsically weak interactions [49], implementing improved field control, and adding a resonant low-finesse cavity as a mode cleaner. Past work has shown [23] that spacetime trajectories can be fully controlled to enable much larger loops, holding at large separations, and executing multiple Bloch oscillations; this means that loop area can in principle grow almost without bound, so any improvements in coherence will directly enhance force sensitivity. The flexibility, power,

and large design parameter space offered by the Floquet engineering framework, along with the excellent match between interferometer performance and both numerical and analytical theory, should allow the use of optimal control and machine learning techniques [50] to design more complex interferometer sequences for enhanced robustness and sensitivity. While the low-mass isotope ^7Li is helpful here for enabling large spatial separation, the technique could be expanded to heavier atoms by using higher-band transitions to generate higher momentum transfer. Finally, given the band-synthesis approach used here, it may be instructive for future developments to compare to, and draw inspiration from, related efforts in driven condensed matter [27, 28].

Acknowledgments

We thank Naceur Gaaloul for useful discussion, and Yifei Bai for physical insight and a critical reading of the manuscript. We acknowledge support from the Army Research Office (W911NF-22-1-0098 and W911NF-20-1-0294), the Noyce Foundation, and the Eddleman Quantum Institute, and from the NSF QLCI program through Grant No. OMA-2016245. E.N.M. acknowledges support from the UCSB NSF Quantum Foundry through the Q-AMASEi program (Grant No. DMR-1906325). NH acknowledges support from the NSF NRT program under grant 2152201.

-
- [1] T. Young, *I. The Bakerian Lecture. Experiments and calculations relative to physical optics*, *Philosophical Transactions of the Royal Society of London* **94**, 1 (1804).
 - [2] LIGO Scientific Collaboration and Virgo Collaboration, *Observation of Gravitational Waves from a Binary Black Hole Merger*, *Physical Review Letters* **116**, 061102 (2016).
 - [3] L. De Broglie, *Recherches sur la théorie des Quanta*, *Annales de Physique* **10**, 22 (1925).
 - [4] L. Marton, J. A. Simpson, and J. A. Suddeth, *Electron Beam Interferometer*, *Physical Review* **90**, 490 (1953).
 - [5] H. Rauch, W. Treimer, and U. Bonse, *Test of a single crystal neutron interferometer*, *Physics Letters A* **47**, 369 (1974).
 - [6] J. Baudon, R. Mathevet, and J. Robert, *Atomic interferometry*, *Journal of Physics B: Atomic, Molecular and Optical Physics* **32**, R173 (1999).
 - [7] Ch.J. Bordé, N. Courtier, F. Du Burck, A. Goncharov, and M. Gorlicki, *Molecular Interferometry Experiments*, *Physics Letters A* **188**, 187 (1994).
 - [8] M. Abe, P. Adamson, M. Borcean, D. Bortoletto, K. Bridges, S. P. Carman, S. Chattopadhyay, J. Coleman, N. M. Curfman, K. DeRose, T. Deshpande, S. Dimopoulos, C. J. Foot, J. C. Frisch, B. E. Garber, S. Geer, V. Gibson, J. Glick, P. W. Graham, S. R. Hahn, R. Harnik, L. Hawkins, S. Hindley, J. M. Hogan, Y. Jiang, M. A. Kasevich, R. J. Kellett, M. Kiburg, T. Kovachy, J. D. Lykken, J. March-Russell, J. Mitchell, M. Murphy, M. Nantel, L. E. Nobrega, R. K. Plunkett, S. Rajendran, J. Rudolph, N. Sachdeva, M. Safdari, J. K. Santucci, A. G. Schwartzman, I. Shipsey, H. Swan, L. R. Valerio, A. Vasonis, Y. Wang, and T. Wilkason, *Matter-wave Atomic Gradiometer Interferometric Sensor (MAGIS-100)*, *Quantum Science and Technology* **6**, 044003 (2021).
 - [9] J. R. Williams, C. A. Sackett, H. Ahlers, D. C. Aveline, P. Boegel, S. Botsi, E. Charron, E. R. Elliott, N. Gaaloul, E. Giese, W. Herr, J. R. Kellogg, J. M. Kohel, N. E. Lay, M. Meister, G. Müller, H. Müller, K. Oudrhiri, L. Phillips, A. Pichery, E. M. Rasel, A. Roura, M. Sbroschia, W. P. Schleich, C. Schneider, C. Schubert, B. Sen, R. J. Thompson, and N. P. Bigelow, *Interferometry of Atomic Matter Waves in the Cold Atom Lab onboard the International Space Station* (2024), arXiv:2402.14685 [atom-ph].
 - [10] T. Schumm, S. Hofferberth, L. M. Andersson, S. Wildermuth, S. Groth, I. Bar-Joseph, J. Schmiedmayer, and P. Krüger, *Matter-wave interferometry in a double well on an atom chip*, *Nature Physics* **1**, 57 (2005).
 - [11] S. Wu, E. Su, and M. Prentiss, *Demonstration of an Area-Enclosing Guided-Atom Interferometer for Rotation Sensing*, *Physical Review Letters* **99**, 173201 (2007).
 - [12] O. Garcia, B. Deissler, K. J. Hughes, J. M. Reeves, and C. A. Sackett, *Bose-Einstein-condensate interferometer with macroscopic arm separation*, *Physical Review A* **74**, 031601 (2006).

- [13] G. D. McDonald, H. Keal, P. A. Altin, J. E. Debs, S. Bennettts, C. C. N. Kuhn, K. S. Hardman, M. T. Johnsson, J. D. Close, and N. P. Robins, *Optically guided linear Mach-Zehnder atom interferometer*, [Physical Review A](#) **87**, 013632 (2013).
- [14] C. D. Panda, M. J. Tao, M. Ceja, J. Khoury, G. M. Tino, and H. Müller, *Measuring gravitational attraction with a lattice atom interferometer*, [Nature](#) **631**, 515 (2024).
- [15] C. A. Weidner and D. Z. Anderson, *Experimental Demonstration of Shaken-Lattice Interferometry*, [Physical Review Letters](#) **120**, 263201 (2018).
- [16] C. LeDesma, K. Mehling, and M. Holland, *Vector atom accelerometry in an optical lattice*, [Science Advances](#) **11**, eadt7480 (2025).
- [17] T. Petrucciani, A. Santoni, C. Mazzinghi, D. Trypogeorgos, F. S. Cataliotti, M. Inguscio, G. Modugno, A. Smerzi, L. Pezzé, and M. Fattori, *Mach-Zehnder atom interferometry with non-interacting trapped Bose Einstein condensates* (2025), [arXiv:2504.17391 \[quant-ph\]](#).
- [18] C. Li, Q. Liang, P. Paranjape, R. Wu, and J. Schmiedmayer, *Matter-wave interferometers with trapped strongly interacting Feshbach molecules*, [Physical Review Research](#) **6**, 023217 (2024).
- [19] M. B. Dahan, E. Peik, J. Reichel, Y. Castin, and C. Salomon, *Bloch Oscillations of Atoms in an Optical Potential*, [Physical Review Letters](#) **76**, 4508 (1996).
- [20] Z. A. Geiger, K. M. Fujiwara, K. Singh, R. Senaratne, S. V. Rajagopal, M. Lipatov, T. Shimasaki, R. Driben, V. V. Konotop, T. Meier, and D. M. Weld, *Observation and Uses of Position-Space Bloch Oscillations in an Ultracold Gas*, [Physical Review Letters](#) **120**, 213201 (2018).
- [21] V. Xu, M. Jaffe, C. D. Panda, S. L. Kristensen, L. W. Clark, and H. Müller, *Probing gravity by holding atoms for 20 seconds*, [Science](#) **366**, 745 (2019).
- [22] M. Holthaus, *Floquet engineering with quasienergy bands of periodically driven optical lattices*, [Journal of Physics B: Atomic, Molecular and Optical Physics](#) **49**, 013001 (2016).
- [23] C. J. Fujiwara, K. Singh, Z. A. Geiger, R. Senaratne, S. V. Rajagopal, M. Lipatov, and D. M. Weld, *Transport in Floquet-Bloch Bands*, [Physical Review Letters](#) **122**, 010402 (2019).
- [24] C. Weitenberg and J. Simonet, *Tailoring quantum gases by Floquet engineering*, [Nature Physics](#) **17**, 1342 (2021).
- [25] K. Sandholzer, A.-S. Walter, J. Minguzzi, Z. Zhu, K. Viebahn, and T. Esslinger, *Floquet engineering of individual band gaps in an optical lattice using a two-tone drive*, [Physical Review Research](#) **4**, 013056 (2022).
- [26] K. E. McAlpine, D. Gochner, and S. Gupta, *Excited-band Bloch oscillations for precision atom interferometry*, [Physical Review A](#) **101**, 023614 (2020).
- [27] D. N. Basov, R. D. Averitt, and D. Hsieh, *Towards properties on demand in quantum materials*, [Nature Materials](#) **16**, 1077 (2017).
- [28] T. Oka and S. Kitamura, *Floquet Engineering of Quantum Materials*, [Annual Review of Condensed Matter Physics](#) **10**, 387 (2019).
- [29] S. Wang, C. Qin, L. Zhao, H. Ye, S. Longhi, P. Lu, and B. Wang, *Photonic Floquet Landau-Zener tunneling and temporal beam splitters*, [Science Advances](#) **9**, eadh0415 (2023).
- [30] L. Zhao, S. Wang, C. Qin, Z. Liu, C. Liu, X. Hu, Y. Li, B. Wang, and P. Lu, *Bloch-Zener oscillation with engineered Floquet energy bands in synthetic temporal lattices*, [Optics Letters](#) **49**, 7028 (2024).
- [31] L. Landau, *Zur theorie der energieübertragung. I*, [Physikalische Zeitschrift der Sowjetunion](#) **1**, 88 (1932).
- [32] L. Landau, *Zur theorie der energieübertragung. II*, [Physikalische Zeitschrift der Sowjetunion](#) **2**, 46 (1932).
- [33] C. Zener, *Non-adiabatic crossing of energy levels*, [Proceedings of the Royal Society of London. Series A, Containing Papers of a Mathematical and Physical Character](#) **137**, 696 (1932).
- [34] A. Cao, C. J. Fujiwara, R. Sajjad, E. Q. Simmons, E. Lindroth, and D. Weld, *Probing Nonexponential Decay in Floquet-Bloch Bands*, [Zeitschrift für Naturforschung A](#) **75**, 443 (2020).
- [35] S. Arlinghaus and M. Holthaus, *Generalized acceleration theorem for spatiotemporal Bloch waves*, [Physical Review B](#) **84**, 054301 (2011).
- [36] S. Kling, T. Salger, C. Grossert, and M. Weitz, *Atomic Bloch-Zener Oscillations and Stückelberg Interferometry in Optical Lattices*, [Physical Review Letters](#) **105**, 215301 (2010).
- [37] A. Zenesini, D. Ciampini, O. Morsch, and E. Arimondo, *Observation of Stückelberg oscillations in accelerated optical lattices*, [Physical Review A](#) **82**, 065601 (2010).
- [38] S. Shevchenko, S. Ashhab, and F. Nori, *Landau-Zener-Stückelberg interferometry*, [Physics Reports](#) **492**, 1 (2010).
- [39] O. V. Ivakhnenko, S. N. Shevchenko, and F. Nori, *Nonadiabatic Landau-Zener-Stückelberg-Majorana Transitions, Dynamics, and Interference*, [Physics Reports](#) **995**, 1 (2023).
- [40] S. E. Pollack, D. Dries, M. Junker, Y. P. Chen, T. A. Corcovilos, and R. G. Hulet, *Extreme Tunability of Interactions in a Li 7 Bose-Einstein Condensate*, [Physical Review Letters](#) **102**, 090402 (2009).
- [41] M. Greiner, I. Bloch, O. Mandel, T. W. Hänsch, and T. Esslinger, *Exploring Phase Coherence in a 2D Lattice of Bose-Einstein Condensates*, [Physical Review Letters](#) **87**, 160405 (2001).
- [42] A. Hilico, C. Solaro, M.-K. Zhou, M. Lopez, and F. Pereira Dos Santos, *Contrast decay in a trapped-atom interferometer*, [Physical Review A](#) **91**, 053616 (2015).
- [43] Since we vary the modulation amplitude and phase and include additional modulation frequencies, the Hamiltonian loses perfect discrete time-translation symmetry, so that in principle the Floquet formalism is no longer applicable. This is why we use the phrase “dressed energy” rather than quasienergy here. Nevertheless, the hybridized dressed bands generated by a temporally local Floquet picture are of great assistance in predicting the dynamics and sensitivity of different modulation schemes.
- [44] T.-S. Ho, S.-I. Chu, and J. V. Tietz, *Semiclassical Many-Mode Floquet Theory*, [Chemical Physics Letters](#) **96**, 464 (1983).
- [45] M. S. Safronova, D. Budker, D. DeMille, D. F. J. Kimball, A. Derevianko, and C. W. Clark, *Search for new physics with atoms and molecules*, [Rev. Mod. Phys.](#) **90**, 025008 (2018).
- [46] J. Murata and S. Tanaka, *A review of short-range gravity experiments in the lhc era*, [Classical and Quantum Gravity](#) **32**, 033001 (2015).
- [47] D. M. Weld, J. Xia, B. Cabrera, and A. Kapitulnik, *New apparatus for detecting micron-scale deviations from newtonian gravity*, [Phys. Rev. D](#) **77**, 062006 (2008).

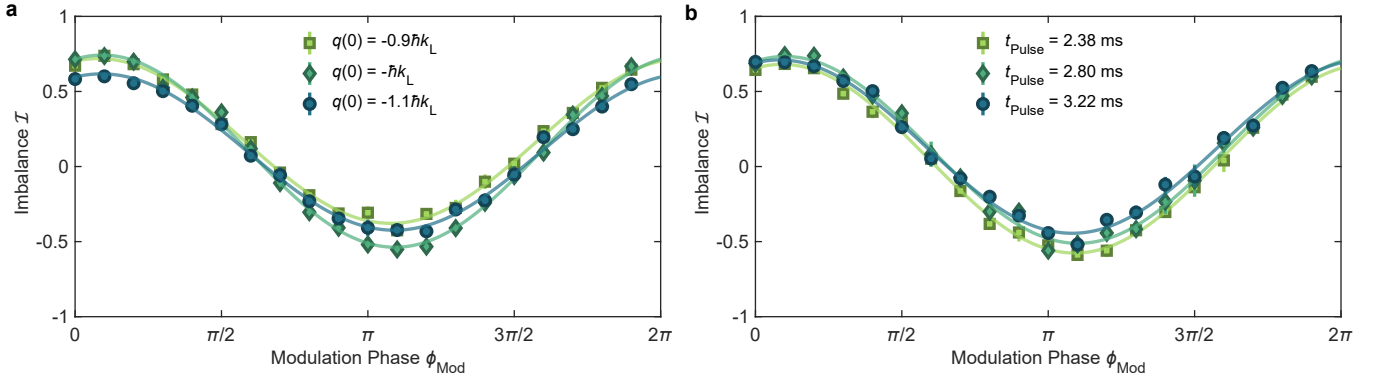
- [48] J. G. Lee, E. G. Adelberger, T. S. Cook, S. M. Fleischer, and B. R. Heckel, New test of the gravitational $1/r^2$ law at separations down to 52 μm , [Phys. Rev. Lett. **124**, 101101 \(2020\)](#).
- [49] X. Zhang, R. P. Del Aguila, T. Mazzoni, N. Poli, and G. M. Tino, *Trapped-atom interferometer with ultracold Sr atoms*, [Physical Review A **94**, 043608 \(2016\)](#).
- [50] C. LeDesma, K. Mehling, J. D. Wilson, M. Nicotra, and M. Holland, *Universal gate set for optical lattice based atom interferometry*, [Physical Review Research **7**, 013246 \(2025\)](#).
- [51] T. N. Ikeda, S. Tanaka, and Y. Kayanuma, *Floquet-Landau-Zener interferometry: Usefulness of the Floquet theory in pulse-laser-driven systems*, [Physical Review Research **4**, 033075 \(2022\)](#).
- [52] D. W. Hone, R. Ketzmerick, and W. Kohn, *Time-dependent Floquet theory and absence of an adiabatic limit*, [Physical Review A **56**, 4045 \(1997\)](#).

Methods

Experimental details. Our experiments begin with a BEC of 2×10^5 ^7Li atoms produced in a horizontal crossed optical dipole trap with trapping frequencies $(\nu_x, \nu_y, \nu_z) = (151.9, 185.0, 239.4)$ Hz. The atoms are prepared in the $|f = 1, m_f = 1\rangle$ ground state, with the magnetic field initially held at 715 G along the vertical z direction to ensure a positive scattering length. The field is then ramped down over 1 s to 543.6 G, where the s -wave scattering length vanishes. Subsequently, the crossed dipole trap is switched off within 200 ms, while a one-dimensional optical lattice with 110 μm waist is simultaneously ramped up (Fig. 1a). This loads the atoms into the ground (S) band of the optical lattice with a narrow quasimomentum spread of $\sim 0.13 \hbar k_L$ (full width at half maximum). Since the lattice is oriented horizontally along the x -axis, gravity does not produce a force along the lattice. Instead, a field gradient $\partial B_z / \partial x$ generated by the coils is ramped up over 38.3 ms, which applies a force and initiates Bloch oscillations. The lattice depth is modulated by varying the radio-frequency power sent to an acousto-optic modulator.

S - P transfer. To perform P - D atom interferometry with magic band structures, the atoms must first be prepared in the P band. This is accomplished via Floquet modulation. After the 38.3 ms field gradient ramp, the atoms acquire a momentum such that the central quasimomentum reaches $q = -\hbar k_L$. A strong lattice amplitude modulation with $\delta V = 1.68 E_R$ is then ramped up within 100 μs , opening up a S - P hybridized gap at $q \sim 0.5 \hbar k_L$. As the matter wave moves towards the Brillouin zone center and traverses the gap, it adiabatically follows the instantaneous Floquet state that connects to the P Bloch band. The modulation is subsequently ramped down within 100 μs , resulting in a near-unity transfer efficiency to the P band. We chose to couple at this quasimomentum to perform our transfer because the perturbation coupling strength $\langle \varphi_{S,q} | \cos^2(k_L x) | \varphi_{P,q} \rangle$ is nonexistent at $q = 0$ and $q = \hbar k_L$ due to the parity selection rules. For this same reason, we use the S and D bands for calibration of lattice depth (Supplemental Information) and do not perform a population inversion (π) at the center of our symmetric P - D interferometer.

Data acquisition and analysis. After band mapping (Fig. 1e), the interferometer output appears as spatially separated atomic clouds corresponding to the P and D bands. We perform standard absorption imaging to obtain the atomic column density. The imaging beam is aligned along the z -axis, and the 5 μs imaging pulse is applied while the magnetic field remains on. To mitigate imaging imperfections, we apply a least-squares regression fringe removal procedure. The P and D band fractions are then calculated by integrating the atom numbers within regions of interest as indicated in Fig. 1e.



Extended Data Fig. 1. **Insensitivity to initial momentum and pulse duration.** (a) Output population imbalance as a function of ϕ_{Mod} for various values of matter-wave quasimomentum $q(0)$ at the beginning of S - P modulation. Apart from the varying quasimomentum, the interferometer protocol is identical to Fig. 4e. The applied force is fixed at $T_B = 10.70$ ms and the interferometer loop size is $0.4\hbar k_L$. (b) Output population imbalance as a function of ϕ_{Mod} for various beamsplitter pulse durations. The applied force and loop size are the same as in (a). As in Fig. 4e, the two modulation pulses are applied symmetrically across the Brillouin zone edge.

Supplementary Information

CONTENTS

1. Floquet-Bloch Atom Interferometry Theory	13
1.1. Bloch Bands in a Static Lattice	13
1.2. Floquet-Bloch Bands in a Driven Lattice	13
1.3. Interferometer Phases	14
2. Magic Depth Calculation	16
3. Numerical Calculation	17
4. Calibration	17
4.1. Lattice Depth	17
4.2. Force	18
4.3. Modulation Depth	18
5. Stabilization	19

1. FLOQUET-BLOCH ATOM INTERFEROMETRY THEORY

In this section, we derive the phase of our Floquet-Bloch atom interferometer from first principles.

1.1. Bloch Bands in a Static Lattice

Consider non-interacting atoms confined in a one-dimensional optical lattice. We assume a periodic boundary condition and a system size L as an integer multiple of the lattice constant, *i.e.*, $L = N\lambda/2$ where N is a large integer and λ is the lattice wavelength. The single-particle Hamiltonian is given by

$$\hat{H}_0 = \frac{\hat{p}^2}{2M} - V_0 \cos^2(k_L \hat{x}), \quad (\text{S3})$$

where M is the atomic mass; V_0 is the lattice depth; $k_L = 2\pi/\lambda$ is the lattice laser angular wavenumber; \hat{x} and \hat{p} are position and momentum operators, respectively. Leveraging the discrete translational symmetry

$$\hat{H}_0(\hat{x} + \lambda/2) = \hat{H}_0(\hat{x}), \quad (\text{S4})$$

Bloch's theorem gives rise to the eigenstates $|\varphi_{n,q}\rangle$, where $n = 0, 1, 2, \dots$ denote Bloch band indices (equivalent to S, P, D, \dots); $q = 2\pi\hbar j/L$ is the quasimomentum; $j = -N/2 + 1, \dots, 0, \dots, N/2$; and \hbar is the reduced Planck constant. In position space, the eigenstates satisfy

$$\begin{aligned} \varphi_{n,q}(x) &= \langle x | \varphi_{n,q} \rangle = \frac{1}{\sqrt{N}} u_{n,q}(x) e^{iqx/\hbar}, \\ u_{n,q}(x) &= u_{n,q}(x + \lambda/2). \end{aligned} \quad (\text{S5})$$

Substituting this ansatz into the time-independent Schrödinger equation results in an eigenvalue problem for the Bloch function $u_{n,q}(x)$:

$$\left[\frac{(-i\hbar\partial_x + q)^2}{2M} - V_0 \cos^2(k_L x) \right] u_{n,q}(x) = E_{n,q} u_{n,q}(x). \quad (\text{S6})$$

This eigenvalue problem can be solved numerically to extract both $u_{n,q}(x)$ and the band energy (band structure) $E_{n,q}$ (Fig. S1a). Notice that if we impose the normalization of $u_{n,q}(x)$ as

$$\int_{-\lambda/4}^{\lambda/4} dx u_{n,q}^*(x) u_{n',q}(x) = \delta_{n,n'}, \quad (\text{S7})$$

the Bloch states are orthonormal:

$$\langle \varphi_{n,q} | \varphi_{n',q'} \rangle = \int_{-L/2}^{L/2} dx \varphi_{n,q}^*(x) \varphi_{n',q'}(x) = \delta_{n,n'} \delta_{q,q'}. \quad (\text{S8})$$

In the following discussion, we take q as a continuous variable, which only makes sense in the $L \rightarrow \infty$ limit.

1.2. Floquet-Bloch Bands in a Driven Lattice

Next, we consider a continuous and sinusoidal amplitude-modulation of the lattice,

$$\hat{H}_{\text{Mod}}(t) = \frac{\hat{p}^2}{2M} - (V_0 + \delta V \cos \omega t) \cos^2(k_L \hat{x}), \quad (\text{S9})$$

where δV and ω are the modulation depth and frequency, respectively. This Hamiltonian exhibits a two-fold (spatial and temporal) translational symmetry that gives rise to the Floquet-Bloch states

$$\langle x | \tilde{\varphi}_{l,q}(t) \rangle = \exp \left[\frac{i}{\hbar} (qx - \tilde{E}_{l,q}t) \right] \tilde{u}_{l,q}(x, t), \quad (\text{S10})$$

where l is the Floquet-Bloch band index, $\tilde{E}_{l,q}$ is the quasienergy, and $\tilde{u}_{l,q}(x, t)$ is the Floquet-Bloch function that satisfies

$$\tilde{u}_{l,q}(x, t) = \tilde{u}_{l,q}(x + \lambda/2, t) = \tilde{u}_{l,q}(x, t + 2\pi/\omega). \quad (\text{S11})$$

Both $\tilde{E}_{l,q}$ and $\tilde{u}_{l,q}(x, t)$ can be obtained from numerically diagonalizing the Floquet Hamiltonian \hat{H}_F , defined as

$$\exp \left(-\frac{2\pi i \hat{H}_F}{\hbar \omega} \right) = \mathcal{T} \exp \left\{ -\frac{i}{\hbar} \int_0^{2\pi/\omega} dt \hat{H}_{\text{Mod}}(t) \right\}, \quad (\text{S12})$$

where \mathcal{T} is the time-ordering operator.

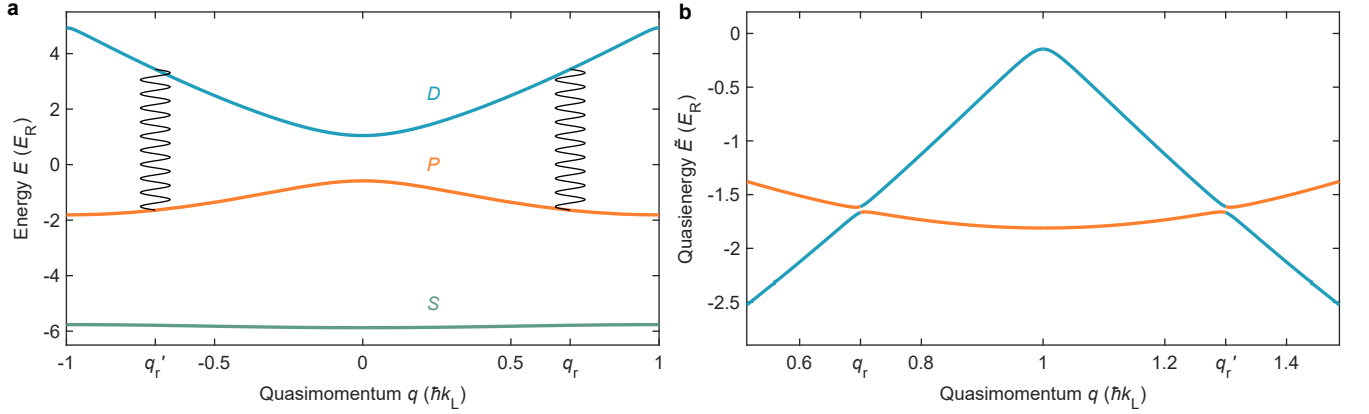


Fig. S1. **Band structure.** (a) The three lowest bands of a static optical lattice, labeled S (green), P (orange) and D (blue). Amplitude modulation couples the latter two bands at the points of resonance q_r, q'_r found by Eq. (S13), indicated by the connecting “drive photons.” (b) Floquet-Bloch bands resulting from the amplitude modulation in (a) hybridizing the P and D bands. Orange and blue indicate the dominant character of the band relative to the original static bands.

It is shown in Fig. S1b that a resonant modulation opens up gaps between two Floquet-Bloch bands. The modulation frequency ω determines the coupled Bloch band indices (n, n') and the resonant quasimomentum q_r , based on the resonance condition

$$E_{n,q_r} - E_{n',q_r} = \hbar \omega. \quad (\text{S13})$$

Meanwhile, the modulation depth δV and the off-diagonal ($n \neq n'$) coupling matrix element govern the size of the gap Δ_{q_r} at the avoided crossings:

$$\Delta_{q_r} \approx \delta V \left| \langle \varphi_{n,q_r} | \cos^2(k_L \hat{x}) | \varphi_{n',q_r} \rangle \right|. \quad (\text{S14})$$

1.3. Interferometer Phases

When a uniform force \mathcal{F} is applied along the lattice direction, the Hamiltonian reads

$$\hat{H}(t) = \frac{\hat{p}^2}{2M} - (V_0 + \delta V \cos \omega t) \cos^2(k_L \hat{x}) - \mathcal{F} \hat{x}. \quad (\text{S15})$$

Applying a gauge transformation $\hat{U} = \exp(-i\mathcal{F}t\hat{x}/\hbar)$, we recover the spatial periodicity,

$$\begin{aligned}\hat{H} &\rightarrow \hat{\tilde{H}} = \hat{U}\hat{H}\hat{U}^\dagger + i\hbar\left(\partial_t\hat{U}\right)\hat{U}^\dagger \\ &= \frac{(\hat{p} + \mathcal{F}t)^2}{2M} - (V_0 + \delta V \cos \omega t) \cos^2(k_L \hat{x}).\end{aligned}\quad (\text{S16})$$

Henceforth, we omit the tilde on $\hat{\tilde{H}}$ and assume \hat{U} is always applied.

We define $\mathcal{Q} = \mathcal{F}t$ as the slowly varying parameter in the Hamiltonian (S16) that facilitates the instantaneous-Floquet-state (IFS) formalism [51]. A set of IFSs $|\tilde{\zeta}_{l,q}(t)\rangle_{\mathcal{Q}}$ can be given by diagonalizing the Hamiltonian (S16) while fixing \mathcal{Q} :

$$|\tilde{\zeta}_{l,q}(t)\rangle_{\mathcal{Q}} = |\tilde{\varphi}_{l,q+\mathcal{Q}}(t)\rangle. \quad (\text{S17})$$

Intuitively, one would imagine that the quantum state can adiabatically follow the IFS when the control parameter \mathcal{Q} varies slowly. However, an exact Floquet adiabatic limit is likely absent due to the dense quasienergy spectrum and infinitely many avoided-crossings from multi-Floquet-photon resonances [52]. We adopt a coarse-graining argument [22], which states that an infinite number of avoided-crossings below a certain scale can be ignored because of the finite experimental time scale. Away from the sizable avoided-crossings, the quantum state $|\psi(t)\rangle$ still adiabatically follows the IFS in an approximate sense,

$$|\psi(t)\rangle \approx e^{-i\phi_{\text{Dyn},l}(t)} |\tilde{\zeta}_{l,q_0}(t)\rangle_{\mathcal{Q}} = e^{-i\phi_{\text{Dyn},l}(t)} |\tilde{\varphi}_{l,q_0+\mathcal{Q}}(t)\rangle, \text{ if } |\psi(0)\rangle = |\tilde{\varphi}_{l,q_0}(0)\rangle, \quad (\text{S18})$$

where

$$\phi_{\text{Dyn},l}(t) = \frac{1}{\hbar\mathcal{F}} \int_{q_0}^{q_0+\mathcal{F}t} dq \tilde{E}_{l,q} \quad (\text{S19})$$

is the dynamical phase. Combined with the periodicity of quasimomentum, Eq. (S18) confirms the presence of Bloch oscillations in Floquet-Bloch bands. To harness the force sensitivity of $\phi_{\text{Dyn},l}(t)$, we introduce interference between two Floquet-Bloch bands via Landau-Zener tunneling [31–33] at avoided-crossings. This occurs when the Bloch frequency $\omega_B = \mathcal{F}\lambda/2\hbar$ is comparable to the gap size Δ_{q_r}/\hbar . As illustrated in Fig. 1c, when a Floquet-Bloch atom in the upper band passes the avoided crossing at $q = q_r$, it splits into a superposition of two Floquet-Bloch waves, and the ratio can be adjusted by tuning δV , and thus the gap size, to realize a 50-50 beam splitter. The two waves accumulate distinct dynamical phases before recombining at the second avoided crossing at $q = q'_r$. This setup forms a Landau-Zener-Stückelberg-Majorana interferometer [38, 39], whose output is measured as the final population distribution between the Floquet-Bloch bands given by the adiabatic-impulse approximation [51]

$$\mathcal{I} \approx 4p(1-p)(1 + \cos \phi_{\text{Int}}), \quad (\text{S20})$$

where L(U) denotes the lower (upper) Floquet-Bloch band;

$$p = e^{-2\pi\delta} \quad (\text{S21})$$

is the Landau-Zener transition probability;

$$\delta = \frac{\Delta_{q_r}^2}{4\hbar v} \quad (\text{S22})$$

is the adiabaticity parameter;

$$v = \mathcal{F} \sqrt{2\Delta_{q_r} \left| \frac{\partial^2 \tilde{E}_{L,q_r}}{\partial q^2} \right|} \quad (\text{S23})$$

is the Landau-Zener sweep velocity;

$$\phi_{\text{Int}} = \phi_{\text{Dyn}} + 2\phi_{\text{Sto}} \quad (\text{S24})$$

is the interferometer phase;

$$\phi_{\text{Sto}} = -\frac{\pi}{4} + \delta(\ln \delta - 1) + \arg \Gamma(1 - i\delta) \quad (\text{S25})$$

is the Stokes phase [38, 39], and

$$\phi_{\text{Dyn}} = \frac{1}{\hbar \mathcal{F}} \int_{q_r}^{q'_r} dq \left(\tilde{E}_{U,q} - \tilde{E}_{L,q} \right) \quad (\text{S26})$$

is the (differential) dynamical phase which is *inversely* proportional to the applied force. Since the Stokes phase ϕ_{Sto} only weakly depends on \mathcal{F} (Fig. S2), the force sensitivity of this interferometer is dominated by the dynamical phase ϕ_{Dyn} , which scales with the energy-momentum area enclosed by the interferometer loop.

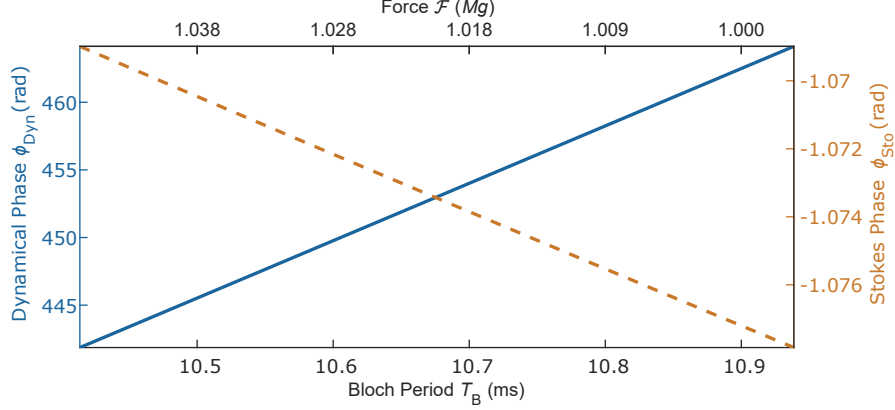


Fig. S2. **Interferometer Phases.** The dynamical (blue, solid) and Stokes (brown, dashed) phases as a function of Bloch period. The lattice and modulation parameters are the same as in Fig. 1. Note the very different y axes for the different phases; the change in the Stokes phase is generally negligible.

2. MAGIC DEPTH CALCULATION

Since the Stokes phase is monotonic in δ and bounded by $[-\pi/2, -\pi/4]$, it varies far less than the dynamical phase for the same range of force and lattice depth. Thus, while exploring the parameter space of V_0 , q_r , and ω , we approximate the magic condition as

$$0 = \frac{\partial \phi_{\text{Int}}}{\partial V_0} \quad (\text{S27})$$

$$= \frac{\partial \phi_{\text{Dyn}}}{\partial V_0} + 2 \frac{\partial \phi_{\text{Sto}}}{\partial V_0} \quad (\text{S28})$$

$$\approx \frac{\partial \phi_{\text{Dyn}}}{\partial V_0} \quad (\text{S29})$$

In addition, since our amplitude modulation is perturbatively weak, static Bloch band energies well approximate the actual Floquet-Bloch band quasienergies. We use numerical integration of these static band energies across the desired quasimomentum range $[q_r, q'_r]$ with sampling resolution 10^3 and numerical differentiation with respect to lattice depth V_0 to estimate the magic condition and the modulation frequency required to couple the P and D bands at the desired quasimomenta. We confirm and refine this prediction with a more sophisticated numerical simulation of Floquet-Bloch bands at a fixed modulation frequency (rather than fixed resonant quasimomentum), as in Fig. 2a. Since both Bloch and Floquet-Bloch bands become flat in the limit of infinite lattice depth, the differential dynamical phase between Floquet-Bloch bands vanishes in the same limit for fixed q_r , precluding the possibility of a local minimum in ϕ_{Dyn} . We instead allow q_r to vary for fixed modulation frequency; consequently, the ϕ_{Int} curves terminate at some minimum and/or maximum lattice depth beyond which the bands are no longer resonant with the modulation for any quasimomentum.

Likewise, numerical calculation of ϕ_{Int} as a function of V_0 and Δq allows estimation of the lattice tolerance in Fig. 3b, defined as the deviation from the magic depth V_0^M resulting in $\phi_{\text{Int}}^M \pm \pi/4$.

3. NUMERICAL CALCULATION

In this section, we describe numerical methods for obtaining energy bands and the magic lattice depth. Using a Fourier mode decomposition for the ansatz wavefunction (S5):

$$u_{n,q}(x) = \sum_j c_{n,q}^{(j)} \exp(2ij k_L x) \quad j \in \mathbb{Z} \quad (\text{S30})$$

Substituting this ansatz into the optical lattice Hamiltonian (S6) gives the eigenvalue equation

$$\sum_{j'} \left[\left(\frac{(2j\hbar k_L + q)^2}{2M} - \frac{V_0}{2} \right) \delta_{j,j'} - \frac{V_0}{4} (\delta_{j-1,j'} + \delta_{j+1,j'}) \right] c_{n,q}^{(j')} = E_{n,q} c_{n,q}^{(j)}, \quad (\text{S31})$$

which can be solved numerically. Using a similar approach to the modulated optical lattice (S9) using Floquet-Bloch waves (S10)

$$\tilde{u}_{l,q}(x, t) = \sum_{n,m} c_{l,q}^{(n,m)} \exp(i(2nk_L x - m\omega t)) \quad n, m \in \mathbb{Z} \quad (\text{S32})$$

results in the eigenvalue equation:

$$\begin{aligned} \tilde{E}_{l,q} c_{l,q}^{(n,m)} = \sum_{n',m'} c_{l,q}^{(n',m')} \left\{ \left(\frac{(2n\hbar k_L + q)^2}{2M} - \frac{V_0}{2} - m\hbar\omega \right) \delta_{n,n'} \delta_{m,m'} \right. \\ - \frac{V_0}{4} (\delta_{n-1,n'} \delta_{m,m'} + \delta_{n+1,n'} \delta_{m,m'}) \\ - \frac{\delta V}{4} (\delta_{n,n'} \delta_{m+1,m'} + \delta_{n,n'} \delta_{m-1,m'}) \\ - \frac{\delta V}{8} (\delta_{n-1,n'} \delta_{m+1,m'} + \delta_{n+1,n'} \delta_{m+1,m'}) \\ \left. - \frac{\delta V}{8} (\delta_{n-1,n'} \delta_{m-1,m'} + \delta_{n+1,n'} \delta_{m-1,m'}) \right\}. \end{aligned} \quad (\text{S33})$$

In practice, $c_{l,q}^{(n,m)}$ and the n, n', m, m' indices can be flattened to produce a vector eigenvalue equation where the eigenvalues are the quasienergies. This method was used along with diagonalizing the effective Floquet Hamiltonian in (S12), and both approaches produced the same numerical results.

4. CALIBRATION

4.1. Lattice Depth

To calibrate the depth of our optical lattice, we perform amplitude modulation spectroscopy on the S and D bands at zero quasimomentum. To do this, we adiabatically load the BEC from the optical dipole trap into the optical lattice (Fig. S3a) and then perform amplitude modulation with a 1 kHz frequency sweep over 2 ms. If the band energy difference between the S and D bands at $q = 0$ falls into the sweep range, atoms will be excited into the D band; after band mapping, the higher-momentum D band atoms are separated from the S band (zero-momentum) atoms to count their relative populations. Scanning the center frequency of this sweep (Fig. S3b) produces a resonance peak, from which we can extract the band energy difference by fitting. Comparison with theoretical predictions of the band gap results in a calibration of our lattice depth with respect to the lattice power PID setpoint (Fig. S3c).

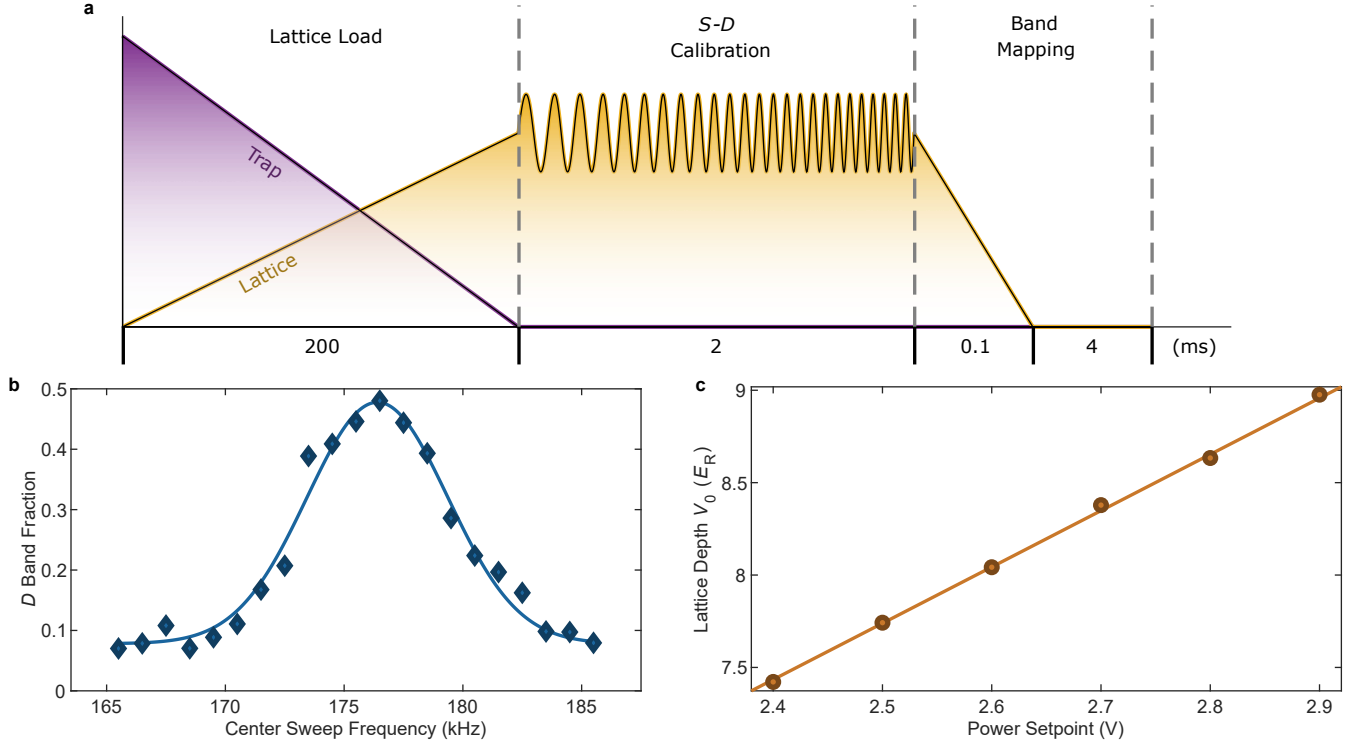


Fig. S3. **Lattice depth calibration.** (a) Experimental sequence for lattice depth calibration. The dipole trap is ramped down and the lattice is ramped up over 200 ms, followed by a resonant amplitude modulation with a 1 kHz frequency sweep over 2 ms. Band-mapping separates the S and D band populations for detection. (b) D band population as a function of center sweep frequency (blue diamonds). A Gaussian fit (blue line) indicates the resonance, which corresponds to the gap between the S and D bands. (c) The experimentally measured band gap is compared to numerical predictions to extract the lattice depth V_0 as a function of lattice power setpoint (rust circles), from which we extract a linear fit (rust line) which determines the horizontal error bars in Fig. 2b.

4.2. Force

To measure the force effecting a Bloch oscillation, it suffices to measure the Bloch oscillation frequency $f_B = 1/T_B = \mathcal{F}/2\hbar k_L$. To do this, we prepare the atoms in the ground band of a deep ($12.3 E_R$) static lattice, initiate a Bloch oscillation with the gradient coils at the chosen setpoint, and measure the quasimomentum using band-mapping after a variable hold time in the lattice. The Bragg scattering at the Brillouin zone edge combined with the nearly-constant dispersion relation of the S band in the deep lattice (tight-binding) limit gives rise to a sawtooth-like dependence of momentum on the lattice hold time (Fig. S4a), from which we can extract the Bloch oscillation frequency. Performing this same measurement across a range of force setpoints results in a linear fit (Fig. S4b) with which to determine the Bloch frequency and thus the real force over the range of setpoints used for the interferometry experiments.

4.3. Modulation Depth

To calibrate the beamsplitting fraction of the two Landau-Zener avoided crossings, we ramp down our P - D modulation once the atoms reach the Floquet-Brillouin zone edge at $q = \hbar k_L$ so that they undergo only the first avoided crossing. We perform the remainder of the normal interferometer experimental sequence and measure the two output port populations. We empirically select the modulation depth for which the output populations are equal, ensuring that both beamsplitters in the full interferometer sequence set the Landau-Zener transition probability $p = \exp(-2\pi\delta) = 0.5$.

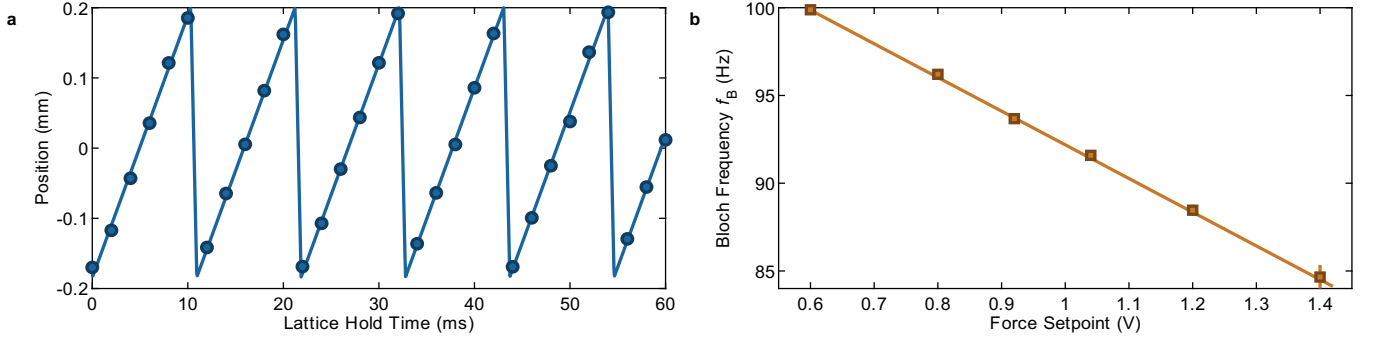


Fig. S4. **Force Calibration.** (a) Fitted atomic positions (blue circles) after band-mapping during a Bloch oscillation with frequency 91.6 ± 0.2 Hz in a static lattice with variable hold time. The triangle-wave fitting curve (blue line) extracts the Bloch frequency. (b) Fitted Bloch oscillation frequency as a function of gradient coil setpoint (rust squares). Vertical error bars result from the aforementioned triangle-wave fits. The linear fit (rust line) determines the horizontal error bars in all the interferometric fringes with respect to Bloch period.

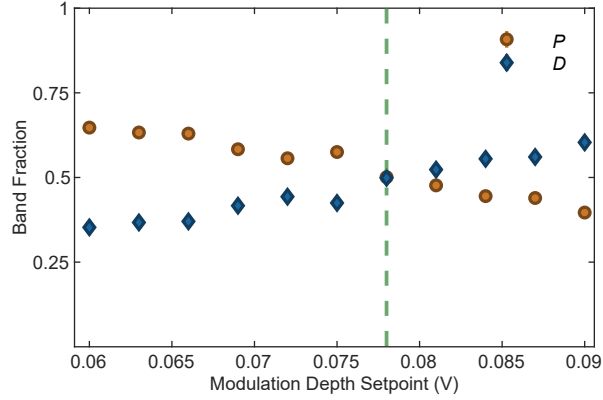


Fig. S5. **Calibration of modulation depth.** Relative P and D band populations after the atoms undergo Landau-Zener tunneling at the first avoided crossing. By scanning the modulation depth, we identify the point at which the population split between the two bands is equal. The green dashed line indicates the calibrated modulation depth $\delta V = 0.35 E_R$, where our Landau-Zener beamsplitter is effectively set to a 50-50 splitting. Measurements taken at a lattice depth of $V_0 = 8.45 E_R$ and modulation frequency 127.4383 kHz. The modulation depth set point is scanned over a range which corresponds to $\delta V = 0.28 E_R$ to $\delta V = 0.40 E_R$.

However, we only calibrate this modulation depth for the magic condition; since we fix δV , the beamsplitting fraction P changes slightly for other lattice depths as a result of changes to $|\varphi_{n,q_r}\rangle$ (see Eq. S14). This undoubtedly accounts for some of the loss in fringe contrast away from the magic condition (Fig. 2b).

5. STABILIZATION

Key parameters of the experiment are actively stabilized during interferometer operation; here we present some details of those feedback loops.

Lattice Laser Power: Our optical lattice beam is produced by an acousto-optic modulator (AOM), so its optical power is controlled by the amplitude of the AOM's RF drive. Since our interferometric phase is sensitive to the lattice depth, we stabilize the laser power using PID feedback from a large-area photodiode. We filter the photodiode output through a 10 kHz low-pass, since the PID is active during our ~ 100 kHz amplitude modulation.

Lattice Laser Pointing: While we do not use a cavity to stabilize our optical lattice mode, we do perform active

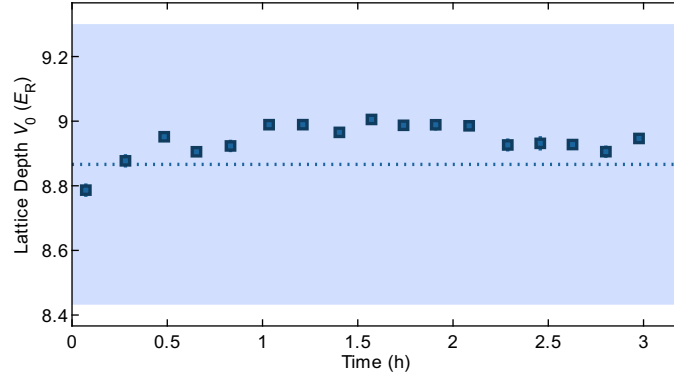


Fig. S6. **Lattice Depth Stability.** Lattice depth as measured by the S - D modulation spectroscopy calibration procedure over three hours (blue squares), compared to the numerically predicted magic depth (blue dotted line) and its $\pm\pi/4$ interferometer phase tolerance (light blue region) for a $\Delta q = 0.4\hbar k_L$ loop. Error bars arise from the fit of the spectroscopy resonance.

drift correction of optical lattice pointing. This is done with an active beam stabilization system from MRC GmbH for the incoming lattice beam and its retroreflection; each beam's position is measured by a position-sensitive device (PSD) sensor and steered by a piezo-actuated mirror mount. Between experimental runs, the optical lattice is flashed on for 250 ms for the MRC PID to recalibrate the pointing of the input and retroreflected beams of the optical lattice, in turn. Careful alignment into the sensors during setup avoids the need to re-align the beams manually. As shown in Fig. S6, the combination of lattice laser power and pointing stabilization gives rise to a stable lattice depth with a drift less than $0.1 E_R$ after the initial warm-up stage. This data set was measured via a series of S - D modulation spectroscopy scans (as demonstrated in Fig. S3) over three hours.

Gradient Coil Current: The force responsible for Bloch oscillations is provided by a magnetic field gradient produced by a coil whose current is actively stabilized. The current is measured by a transducer (Danisense DS50UB-10V) with a feedback loop implemented through a PI controller (Newport LB1005-S). The controller stabilizes the coil's current using a shunt MOSFET (IXYS IXFN140N20P) in parallel with the coil.